Z.B. Szuts and T.B. Sanford. 2013. Vertically averaged velocity in the North Atlantic Current from field trials of a Lagrangian electric-field float. *Deep-Sea Research II*. **85**: 210–219. doi:10.1016/j.dsr2.2012.07.022

Vertically-averaged velocities in the North Atlantic Current from field trials of a Lagrangian electric-field float

Zoltan B. Szuts[a,1,*], Thomas B. Sanford[b]

[a] *Max-Planck-Institut für Meteorologie, Bundesstrasse 53, 20146 Hamburg, Germany.*
[b] *Applied Physics Laboratory and School of Oceanography, University of Washington, 1013 NE 40th Street, Seattle, WA 98105, USA.*

Abstract

A subsurface Lagrangian float that utilizes motional induction to calculate vertically-averaged velocities was tested in the North Atlantic Current (NAC), taking advantage of existing cruises and infrastructure. The Electric Field Float (EFF) is a RAFOS float with horizontal electrodes that measures its own velocity by RAFOS tracking and calculates vertically-averaged velocities when merged with the electrode system. The observations showed depth-averaged velocities that were fast in the core of the NAC (0.6–0.9 m s^{-1}) and moderate in adjacent recirculations and eddies (0.3–0.4 m s^{-1}). A float at 850 dbar moved at close to the depth-averaged velocity, while shallower floats followed surface intensified flow on top of the depth-averaged motion. Integral time scales of depth-averaged velocity (1.3–1.6±0.4 d) are slightly shorter than time scales of float velocity (1.6–2.0±0.3 d), while integral length scales of depth-averaged water velocity (35 ± 10 km for u, 18 ± 6 km for v) are slightly shorter than length scales of float motion (53 ± 12 km for u, 28 ± 6 km for v). Velocity spectra of depth-averaged velocity show significant variance at inertial periods. Quantitative and qualitative validation with multiple independent data sets confirms the accuracy of the instrument and sampling strategy in the NAC, advancing the limited observational knowledge of depth-averaged circulation in subpolar regions.

Keywords: Lagrangian float, Oceanic electric field, Depth-averaged velocity, North Atlantic Current

1. Introduction

The North Atlantic Current NAC connects the subtropical gyre and the Gulf Stream with polar latitudes and is a major pathway in the thermohaline circulation. Downstream from Cape Hatteras, the Gulf Stream changes from a surface intensified current to a flow with significant deep velocities (Johns et al., 1995) by the time it reaches the Grand Banks and feeds into the NAC. Though deep velocities in the NAC were not appreciated historically because of the common assumption of a deep level of no motion, major field programs since the 1990s (Carr and Rossby, 2001; Meinen and Watts, 2000) have yielded detailed measurements of absolute velocity and transports that attest to the strength of the NAC. The depth-averaged flow of surrounding recirculations remains poorly sampled (Bower et al., 2011), especially for eddying motions.

Lagrangian subsurface floats that rely on motional induction were deployed for field trials in the NAC in 1994 (see Figure 1 for regional setting). Their deployment was made possible by the willingness of Tom Rossby to allow shared use of his research cruises. The large research infrastructure in the region — sound sources for the drifting floats and moored velocity measurements for comparison purposes — allowed for a more extensive field trial than would have been possible otherwise and sampled the region north of the Mann Eddy (Figure 1). The data give insight into the dynamics of the region and remain unique and unrepeated measurements. Subpolar regions are widely recognized as having significant barotropic variability, and the ob-

*Corresponding author
Email addresses: zoltan.szuts@zmaw.de (Zoltan B. Szuts), sanford@apl.washington.edu (Thomas B. Sanford)
[1] formerly at the Applied Physics Laboratory and School of Oceanography, University of Washington.

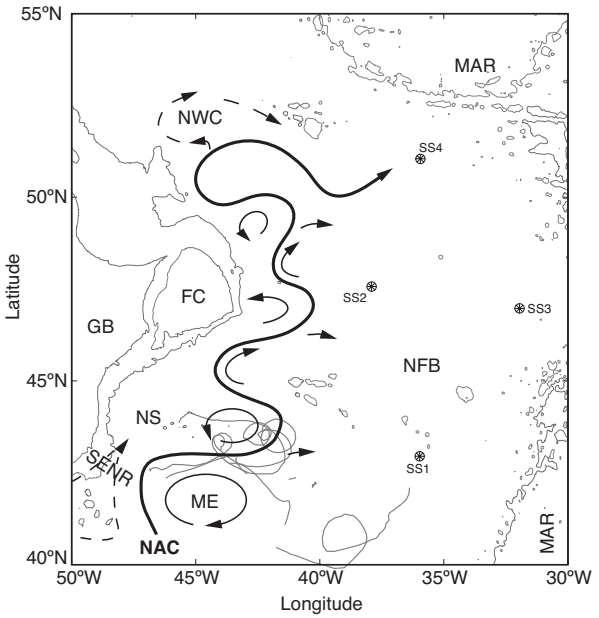

Figure 1: A chart of the North Atlantic showing a schematic of the NAC path with recirculation cells and probable locations of water detrainment from a large deployment of isopycnal RAFOS floats (Rossby, 1996, solid and dashed thick lines with arrows). EFF trajectories are shown in gray. Features labeled are: sound sources used for RAFOS tracking (SS1–SS4); bathymetry contours at 1000 and 3000 m from ETOPO2; NAC, North Atlantic Current; SENR, Southeast Newfoundland Ridge; ME, Mann Eddy; NWC, Northwest Corner; GB, Grand Banks; FC, Flemish Cap; NS, Newfoundland Seamounts; NFB, Newfoundland Basin; and MAR, Mid-Atlantic Ridge.

servations, instrumental techniques, and observational strategies presented here are early efforts to characterize depth-averaged or barotropic dynamics at high latitudes from direct observations.

Three major field projects were active during the EFF deployments that provide data for independent verification and interpretation of the electric field measurement. The projects are a moored current meter array along the Southeast Newfoundland Ridge across the NAC and the Mann Eddy (Clarke et al., 1998; Schott et al., 2004), a line of inverted echo sounders (IES, including some IES's with pressure sensors called PIES) along the same line (Meinen and Watts, 2000), and a deployment of one hundred RAFOS floats (Rossby, 1996).

The current meter and PIES arrays were located near the beginning of the NAC and showed that the time-average absolute transport of the NAC is 140 Sv and has a standard deviation of 40 Sv (Meinen and Watts, 2000), with a range of -60 to 220 Sv (Schott et al., 2004), much larger than previous and contemporaneous calculations of roughly 40 Sv or less that did not have direct velocity measurements (Mann, 1967; Dietrich et al., 1975; Clarke et al., 1980; Krauss, 1986; Krauss et al., 1987; Schmitz and McCartney, 1993; Caniaux et al., 2001). Compared to using absolute reference velocities, assuming deep levels of no motion underestimated transports by 20–60% (Meinen and Watts, 2000; Meinen et al., 2000).

The RAFOS floats (Anderson-Fontana et al., 1996) sampled absolute velocities on two isopycnal surfaces and quantified the effect of the strong eddy field (Zhang et al., 2001; Dutkiewicz et al., 2001). In a time-averaged sense, float velocities were combined with hydrography (Pérez-Brunuis et al., 2004) to yield maps of absolute circulation in the upper 1000 m, further confirming the importance of velocity measurements for calculating time-averaged absolute transport pathways in the region.

Observations of the depth-averaged component in the NAC extension region and in recirculation regions to the east remain sparse. Subsequent observational programs have focused on the downstream extension of the NAC in the subpolar front (Bower and von Appen, 2008), the Deep Western Boundary Current and its deep velocities that are inshore of the NAC (Bower et al., 2009), and on the region of eastward drift that carries water from the NAC across the mid-Atlantic Ridge (Rhein et al., 2011). In these regions of moderate and variable flow, infrequent sampling of barotropic motion is not sufficient to characterize its role in basin-scale circulation.

The article is organized as follows. Motional induction is introduced first (section 2), in order to understand the Electric Field Floats (EFFs, section 3). The EFF deployment in the NAC is described (section 4) and the measurements are validated amongst themselves and with independent data sets (section 5). Finally, we discuss the implications of the observations for the dynamics of the flow field (section 6) before concluding (section 7).

2. Theory of Motional Induction

Though the fully three dimensional theory of electromagnetic fields in the ocean is complex (Sanford, 1971; Chave and Luther, 1990; Szuts, 2012), geophysical scaling of oceanic flows simplifies the

equations into forms that only depend on the vertical dimension and that are used to interpret motional induction observations. The assumption that horizontal length scales are much larger than vertical length scales ($H \ll L$) leads to electric circuits that form in a vertical plane. In so doing, electric fields and electric currents only depend on the vertical dimension and can be considered one dimensional. This approximation is thus called both first order and one-dimensional (1D). For further details on motional induction see the references cited above.

The energy source, the motional induction of salt ions moving through the earth's magnetic field, generates an electromotive force that generates electric fields ($\boldsymbol{E}$), which in turn drive electric currents ($\boldsymbol{J}$) in the water column as described by Ohm's law:

$$-\boldsymbol{E} = \boldsymbol{u} \times \boldsymbol{F} - \boldsymbol{J}/\sigma \tag{1}$$

where σ is the electrical conductivity of seawater and $\boldsymbol{F}$ is the earth's magnetic field. Self-inductive effects are negligible (Sanford, 1971), and the inductive coupling of the ocean with deep but conductive earth interior is minor for subtidal flows with horizontal length scales much smaller than the earth's radius (Chave and Luther, 1990). This leads to a quasi-static assumption that will be used for the remainder of this analysis. In this situation, $\boldsymbol{J}$ arise from the cross product of horizontal velocity $\boldsymbol{u}_h$ and the earth's vertical magnetic field F_z, modified by ocean and sediment conductivities, while the *in situ* horizontal electric field $\boldsymbol{E}_h$ is vertically uniform and depends on the vertically-averaged velocity and the amount of shorting through the sediment. The 1D electromagnetic fields are also averaged horizontally within a few times the effective water depth (Chave and Luther, 1990; Szuts, 2010).

The horizontal electric field $\boldsymbol{E}_h$ can be converted to an equivalent velocity (Sanford, 1971) according to

$$-\boldsymbol{E}_h = \overline{\boldsymbol{u}}^* \times \hat{\boldsymbol{z}} F_z \quad . \tag{2}$$

By invoking conservation of charge, the velocity $\overline{\boldsymbol{u}}^*$ is defined as

$$\overline{\boldsymbol{u}}^* = \frac{\int_{-H}^{0} \sigma \boldsymbol{u}\, \mathrm{d}z}{\int_{-H_s}^{0} \sigma\, \mathrm{d}z} = \left(\frac{1+\gamma}{1+\lambda}\right) \overline{\boldsymbol{u}} \quad . \tag{3}$$

The vertically-averaged or barotropic velocity $\overline{\boldsymbol{u}}$ is

$$\overline{\boldsymbol{u}} = \frac{1}{H} \int_{-H}^{0} \boldsymbol{u}\, \mathrm{d}z, \tag{4}$$

γ is the normalized conductivity-velocity covariance

$$\gamma = \frac{\overline{\sigma' \boldsymbol{u}'}}{\overline{\sigma}\,\overline{\boldsymbol{u}}}, \qquad \text{with} \quad \overline{\sigma' \boldsymbol{u}'} = \frac{1}{H} \int_{-H}^{0} \sigma' \boldsymbol{u}'\, \mathrm{d}z,$$

λ is the sediment conductance ratio

$$\lambda = \int_{-H_s}^{-H} \sigma\, \mathrm{d}z \Bigg/ \int_{-H}^{0} \sigma\, \mathrm{d}z = \frac{(H_s - H)\sigma_s}{H\overline{\sigma}}, \tag{5}$$

H is the depth of the water column, H_s is the bottom of the conducting sediment, σ is the vertically-varying electrical conductivity of the water column, and σ_s is the uniform electrical conductivity of the sediment. The first equality in (3) explicitly shows the vertical averaging of $\overline{\boldsymbol{u}}^*$ over the thickness of the sediment and water columns. The physics of this description is more easily seen in the second equality, however, where the integrals are simplified by a Reynolds decomposition in the vertical (i.e. $f(z) = \overline{f} + f'(z)$) of $\boldsymbol{u}$ and σ and by dividing both numerator and denominator by $\overline{\sigma}H$.

Two factors relate $\overline{\boldsymbol{u}}^*$ to $\overline{\boldsymbol{u}}$: the first factor γ describes covariances in the vertical between $\boldsymbol{u}$ and σ, a baroclinic phenomena; and the second factor λ describes how conductive sediment shorts the oceanic electric field and diminishes $\overline{\boldsymbol{u}}^*$ relative to $\overline{\boldsymbol{u}}$.

In currents that are surface intensified like the NAC, γ is expected to be non-zero: it is quantified in section 5.3.1.

The ratio of sediment conductance to water column conductance (λ) is typically small (0–0.2) in the open ocean, as seen in both models (Chave and Luther, 1990; Flosadóttir et al., 1997; Tyler et al., 1997) and observations (Sanford et al., 1985; Sanford, 1986; Chave and Luther, 1990; Szuts, 2004). In the Newfoundland Basin in water deeper than 4000 m, the sediment is only a few kilometers thick (Tucholke, 1986; Laske and Masters, 1997) and its homogeneity and small conductivity is relatively easy to parameterize for our purposes (Flosadóttir et al., 1997). To interpret the EFFs in terms of absolute velocity $\overline{\boldsymbol{u}}$, we estimate λ heuristically by comparison with geostrophic velocities in section 5.3.2.

The last modification necessary to this theory accounts for measurements taken from a moving platform. If the instrument and its electrodes are themselves moving through the earth's magnetic field, then the apparent or electric field velocity (denoted $\boldsymbol{u}_{\mathrm{EF}}$) calculated from the measured electric field is

the difference between the water motion at that depth level and $\overline{\boldsymbol{u}}^*$:

$$-\boldsymbol{E}_h = (\overline{\boldsymbol{u}}^* - \boldsymbol{u}(z_{\rm instr})) \times F_z \hat{\boldsymbol{z}} = -\boldsymbol{u}_{\rm EF} \times F_z \hat{\boldsymbol{z}} \quad (6)$$

Independent measures of $\boldsymbol{u}(z_{\rm instr})$ thus enable $\overline{\boldsymbol{u}}^*$ to be calculated. Because $\overline{\boldsymbol{u}}^*$ as a close-approximation to the vertically-averaged velocity in this region, and $\boldsymbol{u}(z_{\rm instr})$ as the water velocity at a given depth, then their difference is an approximation to the baroclinic velocity at that depth. We define barotropic velocity as the vertically-averaged velocity and note that alternate definitions of barotropic have been used previously in some studies of the Gulf Stream and NAC. Thus, the ratio of $|\boldsymbol{u}_{\rm EF}|$ to $|\overline{\boldsymbol{u}}^*|$ is a rough indication of the ratio of baroclinic to barotropic speeds.

3. Electric Field Floats

The Electric Field Float (EFF) is a commercial RAFOS float (Bathy Systems, Inc) modified to measure 2-D horizontal electric fields (Figure 2). The float measures absolute electric fields while spinning about its axis, which it then combines with positioning from the RAFOS system to calculate depth-averaged velocities. For the NAC deployment, these floats were programmed to descend to a target pressure, sample for 45 days, and then rise to the surface to transmit their data. Floats of this type can additionally be programmed to follow isopycnals or to profile vertically at specified intervals, such as the standard ARGO sampling pattern of drifting at depth for 10 days before profiling from 2000 m to the surface. A more recent variation of the EFF, the Electromagnetic APEX float (EM-APEX, Sanford et al., 2007; Sanford et al., in press), though also capable of calculating $\overline{\boldsymbol{u}}^*$ by utilizing surface GPS fixes, does not use a dedicated subsurface tracking system.

The EFF consists of two systems: a RAFOS system and an electric field (EF) system. The RAFOS system performs underwater acoustic tracking and end-of-mission data telemetry. More details about RAFOS floats can be found in (Rossby et al., 1986), and the concurrent deployment in the NAC is described by Anderson-Fontana et al. (1996). Minor modifications were made to the basic RAFOS setup to allow communication and coordination with the EF system.

The EF system is composed of two pairs of electrodes, external housing, rotation vanes, a gimbaled fluxgate compass, and other electronics (Figure 2). External components are made of electrically inert material to minimize external corrosion currents. Electrodes are connected to the ocean at the end of saltwater-filled tubes, giving an effective electrode separation of 1 m that does not distort the ambient electric field (Sanford et al., 1978). Agar in the end of the tubes minimizes electrode drift and prevents air from entering during deployment. The vanes rotate the float and periodically change the orientation of the electrodes to allow removal of electrode self-potentials. In the relatively stable environment below the thermocline, a few rotations per measurement period are sufficient to remove the time-varying electrode offsets. The electrodes and compass are sampled every 2 minutes with digital resolution of 0.153 μV, equivalent to 0.0033 m s^{-1} in the NAC, and 0.4° internally (1.5° stored). Pressure and temperature are sampled every 6 minutes. The instrument is described in more detail in Sanford et al. (1995) and Szuts (2004).

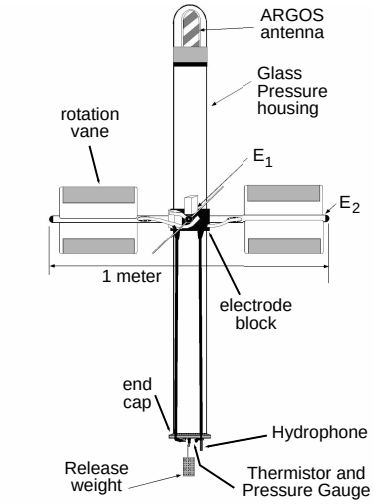

Figure 2: The Electric Field Float (EFF). The cylindrical glass housing is the base RAFOS float. Electrode arms (labeled E_1 and E_2), an electrode block, rotation vanes, and cables from the electrodes to the end cap, are added externally to allow high quality measurements of the ambient electric field.

The data processing involves two steps: converting the RAFOS tracking to geographic positions, and combining the float velocity with the electric field velocity.

RAFOS tracking is described in detail in other sources (Rossby et al., 1986): this involves converting the time of arrival from a sound source into a range, and combining multiple ranges into a hori-

zontal location. The NAC sound sources emitted a signal twice per day at a pre-determined time. Since the EFFs received signals from three sound sources (sound sources 1, 3 and 4) and never crossed the center-line between any two sound sources, hyperbolic tracking could be used which gave one degree of freedom in the calculated position. The tracking was performed using the same methods, programs, and sound source clock drifts as used for the large RAFOS float deployment in this region Anderson-Fontana et al. (1996).

Gaps in position of 5 or less consecutive sampling times (equivalent to 2.5 days) were interpolated across with cubic spline interpolation. Float or RAFOS velocities $\boldsymbol{u}_{\mathrm{RAF}}$ were calculated as the centered difference between positions 24 hours apart.

The EF variables were processed internally every 4 hours before being saved to internal memory. Temperature and pressure were simply averaged, and the total count of clockwise and counterclockwise half-turns was recorded. A least squares fit extracted the oceanic electric field from sensor drift by fitting the data to a function of the form

$$\Delta_h\phi = a_0 + a_1 t + a_2 t^2 + a_3 \sin\theta + a_4 \cos\theta \quad , \quad (7)$$

where $\Delta_h\phi$ is the measured potential, $a_0 \ldots a_4$ are the coefficients to be fitted, t is time, and $\theta(t)$ is the orientation of the electrode arms relative to magnetic north at each measurement time. The mean, linear, and quadratic (a_0, a_1, a_2) terms remove drift in the electrode self-potential, and horizontal electric field in geomagnetic coordinates is given by a_3 and a_4. This fitting procedure is performed on each electrode arms separately.

The float's rotation is essential for removing the electrode self-potential (order 1 mV) from the oceanic signal (order 1 μV). If there is insufficient rotation, then the last two basis functions will not be sufficiently orthogonal, and the linear inversion will be ill-conditioned and give large errors. This is diagnosed by storing a unit-less quantity $R_{\max}$ that is the maximum off-diagonal correlation of the basis functions for each fitting period. Sanford et al. (1993) found that if $R_{\max} \leq 0.85$, then calculated velocity from the two electrode pairs had an rms error less than 0.01–0.02 m s^{-1}. The float can be rotated by internal waves, which rotate the float equally clockwise and counter clockwise, or by mean vertical water motion, which produces a net cumulative rotation. Although floats have previously been constructed to measure vertical water velocity by this same mechanism (e.g. Webb and Worthington, 1968; Lherminier, 1998), for the EFF it is an ancillary measurement that arises from the need to remove electrode self-potentials. For slow vertical velocities, each half-rotation of an EFF corresponds to 1.09 m of vertical rise (Szuts, 2004).

Table 1: Velocities used in the manuscript, with reference equation number. The vector form is shown (in bold, $\boldsymbol{u}$), and the zonal (u) and meridional (v) components take the same subscripts.

symbol	description
$\boldsymbol{u}_{\mathrm{RAF}}$	float velocity from RAFOS tracking
$\boldsymbol{u}_{\mathrm{EF}}$	velocity derived from electric field, (6)
$\overline{\boldsymbol{u}}$	vertically-averaged velocity, (4)
$\overline{\boldsymbol{u}}^*$	conductivity-weighted vertically-averaged velocity, (3)

For calculating $\overline{\boldsymbol{u}}^*$, the electric fields were converted to $\boldsymbol{u}_{\mathrm{EF}}$ following (6), were binned and averaged to the 12-hourly RAFOS velocities, and were combined with $\boldsymbol{u}_{\mathrm{RAF}}$ after (6). The earth's magnetic field F_z is taken as a constant and is calculated from (Macmillan et al., 2003). All velocities calculated by the EFF are listed in Table 1.

4. North Atlantic Current Deployment

Four EFFs were deployed by Sandy Fontana (URI) in the North Atlantic in late October 1994 during CSS *Hudson* cruise 94030 (R. Allyn Clarke, chief scientist). All floats were released in a strong eastward flow; floats 7 and 10 were NW of the Mann Eddy, while floats 8 and 9 were 200 km further downstream and N of the Mann Eddy. Equilibration depths were approximately 500 m for float 7, 150 m for float 8, and 850 m for floats 9 and 10.

After sampling for roughly 45 days, all floats surfaced on December 9 and transmitted their data for 2 months, except for float 10 which became quiet after 4 days on the surface. Problems at Service Argos resulted in the first 2 weeks of data being scrambled irreversibly, after which the problem was corrected and the initial data unscrambled as much as possible, recovering an additional 20–30% of data. Strong winds (typically 30 knots) and stormy weather in December 1994 further reduced the quality of data transmissions. Of the 4 floats, floats 7 and 8 have a couple of gaps in their time series, float 9 has a nearly continuous record, and

float 10 has 40% of its record. The data are presented in detail in Szuts (2004). Vertically-averaged velocities $\overline{\boldsymbol{u}}$ are calculated from $\overline{\boldsymbol{u}}^*$ using the values of λ and γ calculated in section 5.

The EFFs dispersed rapidly after deployment (Figure 3). All of the floats were deployed in an eastward flowing branch of the NAC that attained speeds of 0.5–1 m s^{-1} at the float depths and vertically-averaged speeds of 0.6–0.9 m s^{-1}. One shallow (EFF 8 at 150 dbar) and one deep float (EFF 10 at 850 dbar) were detrained from the NAC and ended their deployment in the poorly structured flow regime to the east that showed speeds of 0.05–0.2 m s^{-1} for $\overline{\boldsymbol{u}}$, consistent with their deployment seaward of the center of the NAC (as defined by where the 10°C isotherm crosses 450 dbar, Meinen, 2001). EFF 8 experienced significant surface-intensified baroclinic motions, as indicated by values of $|\boldsymbol{u}_{\rm EF}| \,/\, |\overline{\boldsymbol{u}}^*|$ of 1–3 or larger. The two other floats, EFFs 7 at 500 dbar and 9 at 850 dbar, were carried to the north around a stationary meander of the NAC. The shallower one was caught in a stationary eddy field with speeds of 0.15–0.4 for $\overline{\boldsymbol{u}}$, whereas the deeper float detrained on the inshore side of the NAC and was headed toward the Newfoundland Seamounts at the end of its mission. The longer journeys of EFFs 7 and 9 along the NAC were consistent with their being placed close to the central axis of the NAC.

The shallower floats often had a larger $\boldsymbol{u}_{\rm RAF}$ than $\overline{\boldsymbol{u}}^*$, suggesting that baroclinic velocities at those depths were larger than the barotropic velocities, while at 850 m the barotropic velocities dominated. Though data returns are not complete, these isobaric floats did not show a consistent vertical water motion at all depths as a float approached or exited an eddy, in contrast to the coherent results of Bower and Rossby (1989). Unfortunately no two floats sampled the same eddy, and so we cannot generalize these observations.

5. Validation of Data

The data quality from the EFF floats can be validated in numerous ways. First, the errors in individual systems can be combined into an expected error. More heuristic measures, however, compare the measurements between two floats, or between floats and simultaneous independent measurements.

5.1. Error Analysis of the Instrument Components

The velocities from the EF and the RAFOS systems can be given independent accuracies, and the errors propagated for $\overline{\boldsymbol{u}}^*$.

The most significant source of error for RAFOS positioning is clock drift in the sound sources and the floats. Sound source clock corrections determined by T. Rossby were applied, and the use of hyperbolic tracking removed the impact of EFF clock drifts (Anderson-Fontana et al., 1996). Position errors are < 3 km from geometric arguments (Szuts, 2004), which are consistent with previous studies (Boebel and Barron, 2003; Carr and Rossby, 2001) that calculated velocity accuracy to be 0.01–0.02 m s^{-1}.

Errors in the EF system can come from (1) electrode or amplifier noise, (2) compass misalignment, or (3) the accuracy of the demodulation processing.

The electrical system was found to have an error less than 0.002 m s^{-1}, the same order as that introduced by digitizing the signal.

The compass deviations of the floats were measured at the NOAA Sand Point, Seattle compass range, and were included in the program the floats ran while deployed. A second check on the compass accuracy is whether, during transits around eddies, significant divergence is observed by the line integral of velocity. Floats 7 and 8 made full transits around eddies, and the divergent velocities are 0.06 m s^{-1} and 0.02 m s^{-1} out of transit velocities of 0.25–0.50 m s^{-1} and 0.40 m s^{-1}, respectively. These speeds are small compared to the transit velocities and point in the same direction as the mean flow, and so are consistent with velocities expected for eddy translation. There is no indication of compass errors.

The inversion of (7) is accurate within 0.01–0.02 m s^{-1} for the cutoff $R_{\rm max}$ chosen. The error is typically much smaller as $R_{\rm max}$ was below 0.4 for most floats and below 0.6 for the shallowest float, so a demodulation error of 0.02 is an upper bound.

The accuracy of the RAFOS velocity is the same as for the EF velocity, and so, assuming independence, a combined error or 0.02–0.03 m s^{-1} is expected.

5.2. EFF Intercomparisons

The precision of $\overline{\boldsymbol{u}}^*$ can be seen by comparing measurements taken when two floats are close together. When close, differences will be due to instrumental sources, while when distant oceanic variability will dominate.

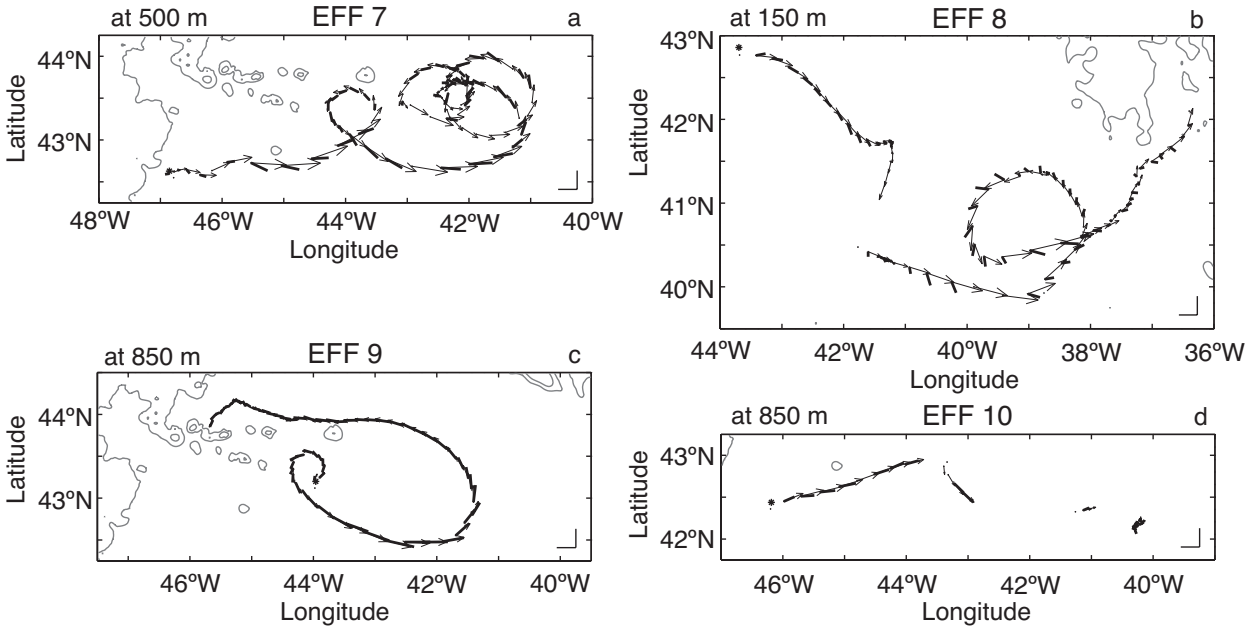

Figure 3: The trajectories and velocities at 12 hour intervals for all EFFs: (a) float 7, (b) float 8, (c) float 9, and (d) float 10. The launch positions are indicated by $*$, $\boldsymbol{u}_{\mathrm{RAF}}$ by the thin arrows, and $\overline{\boldsymbol{u}}^*$ by the thick lines. Velocity scales of 0.5 m s^{-1} are shown in all figures at the bottom right (u and v scales are the same), all plots are at the same geographic scale (but note that the geographic extent differs), and bottom contours are at 3000 and 4000 m (Smith and Sandwell, 1997). All float trajectories are displayed together in Figure 5, and the equilibrium depth of each float is given in the figure.

At small spatial scales, turbulence is dominant over mean flow and rms velocity difference grows quickly with separation, while at larger scales the organized flow dominates and the growth of rms velocity decreases. The EFFs were deployed far enough apart (10s of km) and sampled infrequently enough (every 12 hours) that only the organized flow or random-walk regime is resolved. Specifically, we expect to find the same linear regime for square turbulent float velocities as found by Zhang et al. (2001).

All float measurements within 1 day were selected and the rms differences was binned versus separation distance (Figure 4). The 1-day limit is less than the integral time-scale calculated later. The rms velocity difference is consistent equally well with structure functions of $t^{1/2}$ (Taylor, 1921) or t (Zhang et al., 2001), which are expected for the random-walk regime based on theoretical and observational results, respectively. Each bin has at least 10 or more data points (Figures 4b).

At zero separation in time and space the rms velocity difference provides an upper bound on the float accuracy ($< 0.07 \pm 0.03$ m s^{-1}). Given that the

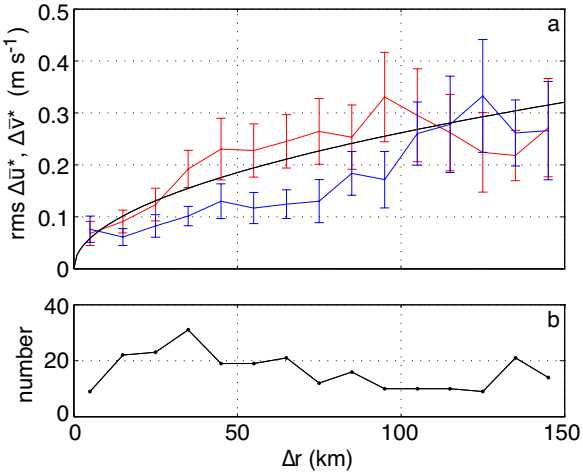

Figure 4: (a) The rms $\Delta\overline{\boldsymbol{u}}^*$ versus separation (Δr) between measurements, with the standard error of the mean being shown by the error bars. The $\overline{u}^*$ component is red, and $\overline{v}^*$ is blue. The black line shows a $\Delta r^{1/2}$ dependence, as reference for a random-walk regime (Zhang et al., 2001). (b) The number of data points per bin, with each separation bin only including data collected 1 day apart or less.

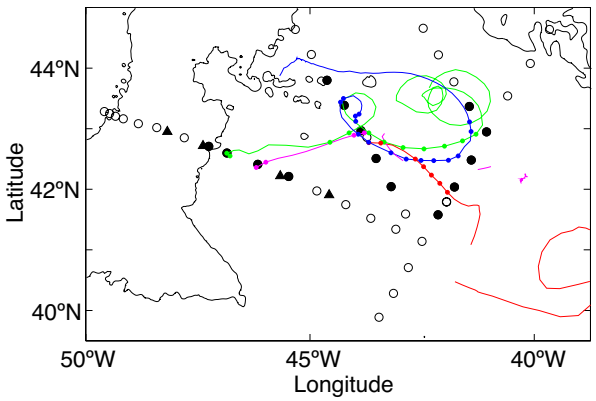

Figure 5: Additional data sets. CTD stations are shown as ○, and those stations used are shown as ●. PIES sensors are shown by ▲. EFF trajectories are shown for EFF 7 (green), 8 (red), 9 (blue), and 10 (magenta), with specific data points used shown by small dots. The 500 and 4000 m isobaths are shown (Smith and Sandwell, 1997).

binning required data up to a day apart to obtain enough data for each bin, the zero-separation rms velocity (the y-intercept) also contains an oceanic signal from the turbulent eddy field.

By comparison, Zhang et al. (2001) find mean square velocity difference for $\boldsymbol{u}_{\mathrm{RAF}}$ of 0, 0.08, and 0.12 m s^{-1} for time separations of 0, 0.5, and 1 day. Each of these 3 time separations is evenly represented in the smallest separation bin in Figure 4. Averaging these three $\boldsymbol{u}_{\mathrm{RAF}}$ values gives an expected oceanic variability of 0.07 m s^{-1}. The variability of $\overline{\boldsymbol{u}}^*$ is expected to be no larger than that of $\boldsymbol{u}_{\mathrm{RAF}}$. Thus, much of the rms velocity difference for $\overline{\boldsymbol{u}}^*$ at zero lag can be expected to be oceanic. Assuming half of the variance is instrumental (0.05 m s^{-1}) and dividing by $\sqrt{2}$ to account for the subtraction of two measurements, yields an accuracy for a single EFF measurement of $\overline{\boldsymbol{u}}^*$ of 0.035 m s^{-1}. This value is consistent with that found in section 5.1.

5.3. Comparisons to Absolute Geostrophic Velocities

Hydrographic data collected close to the floats' deployment (Meinen and Watts, 2000) allows a comparison between the float velocities and those calculated by the geostrophic method. The two techniques are comparable in that both are integrative ways to calculate the velocity that involve horizontal spatial averaging (Luther and Chave, 1993). The hydrographic data also allow calculation of γ and λ for converting $\overline{\boldsymbol{u}}^*$ to $\overline{\boldsymbol{u}}$.

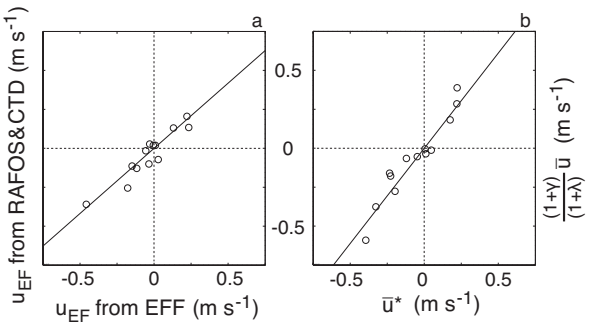

Figure 6: EFF data compared to absolute geostrophic velocities. (a) The RAFOS/CTD-derived right-hand side of (8) plotted against the EFF-derived left-hand side. (b) EFF-measured $\overline{\boldsymbol{u}}^*$ plotted against the same quantity calculated from $\boldsymbol{u}_{\mathrm{RAF}}$-referenced geostrophic velocities.

Float trajectories were chosen that went between two hydrographic profiles within a reasonable amount of time (Figure 5). The amount of time depends on the flow regime: if the flow was fast or changing quickly smaller time differences were accepted than for stable and slow currents (average difference of 4.3 ± 4.1 days). This difference is twice the integral time-scale calculated by Zhang et al. (2001, 1.6–2.0 days), but is necessary to obtain enough points for statistical accuracy. Averages of 2–3 data points were calculated from the EFF velocities to minimize tidal aliasing. Only the component of velocity resolvable by geostrophic calculations (denoted as u) can be compared.

The clearest test for $\overline{\boldsymbol{u}}^*$ would be to plot EFF-derived $\overline{\boldsymbol{u}}^*$ against a similar quantity calculated from absolute geostrophic velocities. Both the EFF $\overline{\boldsymbol{u}}^*$ and the absolute geostrophic velocities depend on $\boldsymbol{u}_{\mathrm{RAF}}$, however, and so are not independent.

A non-standard quantity is defined that can be independently calculated from the EFF electromagnetic measurements and from a combination of RAFOS and geostrophic data. The right hand side of (6) is rewritten using (3) as

$$u_{\mathrm{EF}} = u_{\mathrm{RAF}} - \left(\frac{1+\gamma}{1+\lambda}\right)\overline{u}_{ag} \qquad (8)$$

where γ is calculated from the geostrophic shear and the conductivity profiles of the CTD. The absolute depth-averaged velocity $\overline{u}_{ag}$ is calculated by using u_{RAF} as a reference velocity for the geostrophic velocity profile $u_g(z)$

$$\overline{u}_{ag} = \overline{u}_g - u_g(z_{\mathrm{float}}) + u_{\mathrm{RAF}} \quad .$$

The only undetermined parameter on the right

hand side of (8) is λ, which is tentatively taken to be 0.2 based on later analysis.

A linear regression of the two sides of (8) shows a slope indistinguishable from linear with a correlation coefficient R^2 of 0.88 (Figure 6a). The quality of fit is not altered by different but sensible choices for λ, whether a constant value of 0.1 or values interpolated from bottom sediment conductance maps of Flosadóttir et al. (1997) or Tyler et al. (1997). Despite separations in time between the CTD profiles and float positions, the three data sets (EF, RAFOS, and CTD) are consistent with each other in the theoretically expected manner.

A regression of both sides of (3) using the hydrographic quantities calculated above, namely $\overline{u}^*$ and $(1+\gamma)/(1+\lambda)\,\overline{u}_{ag}$, allows determination of the sediment factor λ (Figure 6.b). The two velocities agree well with each other ($R^2 = 0.92$), and the slope $1+\lambda$ is found to be 1.2 ± 0.1, or $\lambda = 0.2 \pm 0.1$.

The good agreement between the EFFs and geostrophic velocities confirms the assumptions behind them, both in the theoretical description of how oceanic electric field relates to velocities, and in the assumption that the $\boldsymbol{u}_{\mathrm{RAF}}$-referenced geostrophic velocities are an accurate description of the total oceanic velocity. The rms deviation of $\overline{u}^*$ from the linear fit (0.07 m s^{-1}) likely includes a significant fraction from non-coincidence of sampling in both time and space and is similar in magnitude to the differences found between EFFs in the previous subsection.

5.3.1. Velocity-Conductivity Covariance

The velocity-conductivity correlations γ calculated from the hydrographic profiles (Figure 7) describe the fraction by which $\overline{\boldsymbol{u}}^*$ is different from $\overline{\boldsymbol{u}}$ because of baroclinic structure in the water column. The sign of γ indicates whether velocity and conductivity are positively or negatively correlated. Though γ can be large (up to ± 0.5), its importance is determined by the correction to $\overline{\boldsymbol{u}}$ in m s^{-1}, calculated as $\gamma\overline{\boldsymbol{u}}$ or $\overline{\sigma'\mathbf{v}'}/\overline{\sigma}$. The correction is less than 0.02 m s^{-1} in all cases, since large values of γ tend to occur for small $\overline{\boldsymbol{u}}$. Because $\gamma\overline{u}$ does not depend on knowledge of an absolute velocity profile, it can also be calculated from pairs of hydrographic profiles (Chave and Luther, 1990). Close to the axis of the NAC it is $<$0.02 m s^{-1}, while away from the NAC it is 0.005 m s^{-1} or smaller. The error in EFF-derived velocities arising from imprecise knowledge of γ is the same magnitude as other errors. It will not be considered further when converting $\overline{\boldsymbol{u}}^*$ to $\overline{\boldsymbol{u}}$.

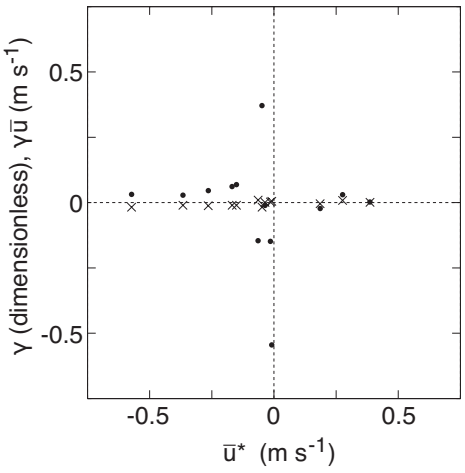

Figure 7: Velocity-conductivity covariance calculated from absolutely referenced geostrophic velocity profiles and hydrographic data. The quantity γ is shown by small dots, and $\gamma\,\overline{u} = \overline{\sigma' u'}/\,\overline{\sigma u}$ by crosses.

These results are consistent with those of Chave and Luther (1990), who found that the first baroclinic mode in the Atlantic has only a few percent effect on $\overline{\boldsymbol{u}}^*$, or that, from POLYMODE, the first baroclinic effect is 7–9% of that of the barotropic mode. In the surface intensified NAC, with the baroclinic correlation factor being less than 0.02 m s^{-1} and with speeds of $\overline{\boldsymbol{u}}$ being 0.25–0.6 m s^{-1}, the effect of baroclinic structure on $\overline{\boldsymbol{u}}^*$ is 3–8% of the depth-averaged velocity.

5.3.2. Bottom Sediment Conductance

Because of the limited region sampled by the EFFs, the single value of λ found above (0.2 ± 0.1) is used to convert $\overline{\boldsymbol{u}}^*$ to $\overline{\boldsymbol{u}}$ for the EFF data This value agrees with independent efforts. From a global circulation and electromagnetic model with 1° resolution using observed sediment thicknesses, (Tyler, personal communication, 2003) calculated λ to be 0.02–0.1 in the deployment region. An electromagnetic model of the North Atlantic by Flosadóttir et al. (1997), also with 1° resolution, found similar variability for λ with magnitudes of 0.06–0.2.

5.3.3. Additional electric field sources

Electric signals in the ocean can also arise from magnetic disturbances in the upper atmosphere. Intense ionospheric fluctuations, often called magnetotelluric storms, are characterized by global length scales, most energy at periods less than 2 days, and polar intensification. The strength

of magnetotelluric activity during the EFF missions, as given by the Kp-index (data obtained from the NOAA National Geophysical Data Center), is mostly lower than 3 and shows a few minor magnetotelluric storms (Kp ≥ 4) that each last for less than a day. The standard deviations of $\boldsymbol{u}_{\mathrm{EF}}$ during the 4-hour internal processing intervals (0.02–0.04 m s^{-1}) are not significantly correlated with the K-index over the course of data sampling. Averaging signals over 4 and 12 hour bins further acts to reduce the influence of ionospheric noise. Because high frequency electromagnetic signals dissipate in the ocean with short skin depths, the deeper floats are better shielded from ionospheric signals than the shallower floats.

5.4. Comparison to PIES/GEM Velocities

The floats were launched along a transect that was instrumented with pressure-equipped inverted echo sounders (Meinen and Watts, 2000), which provide another independent velocity measurement for validation purposes. As the floats quickly moved away from their launch positions there are only 3 instances that the floats are close enough to the array. The 3 comparisons show rms differences in RAFOS velocities of 0.10 m s^{-1}, while those in vertically averaged velocity are 0.06 m s^{-1}. These values are consistent with the results found in previous sections.

6. Results

Our observations of oceanic electric fields the NAC are unique and characterize the nature of depth-averaged or barotropic flow in the region.

6.1. Depth-averaged velocity

The depth-averaged velocities calculated by the EFFs are large but consistent with other measurements nearby. Previous reports of strong depth-averaged flow were suggested: by Carr and Rossby (2001) and Zhang et al. (2001) from the similarity of observations on $\sigma_\theta = 27.2$ and 27.5; by Salmon (1980) from the fact that the potential energy cascade in the NAC would create barotropic velocity components; by Meinen (2001) from absolutely-referenced geostrophic velocities; and by Schott et al. (2004) from direct velocity measurements. Depth-averaged velocities were smaller than velocities in the upper 1000 m but were of similar magnitude. Just upstream from where the EFFs were deployed, an array of PIES calculated an average velocity structure over 19 months (Meinen, 2001), which shows a maximum speed in the upper 500 m of 0.6 m s^{-1}. Instantaneous data (Meinen, 2001; Schott et al., 2004) revealed a large variability in current structure: depth-averaged velocities were typically 0.1–0.3 m s^{-1}, with peaks in the NAC of 0.4 m s^{-1} to the north and in the Mann eddy of -0.23 m s^{-1} to the south. Kearns and Rossby (1998) found that in 1994 the amplitude of the trough at 43°N was very large, with similar positions being observed only 5% of the time over the past 80 years. Thus, the EFFs sampled a particularly strong branch of the NAC on one side of the Mann Eddy, with some of the down-stream eddy field.

The depth-averaged velocities measured by the EFFs are consistent with other transport measurements. The EFFs consistently observed a depth-averaged velocity of 0.6 m s^{-1}. Taking this value as the maximum jet velocity and assuming a triangular cross section with a width of 100 km (Kearns and Rossby, 1998; Meinen, 2001; Zhang et al., 2001) yields an absolute transport of 140 Sv. Nearby arrays of PIES (Meinen and Watts, 2000) and current meters (Schott et al., 2004) found similar transports of 110-140 Sv and 140 Sv, respectively.

There are also other electric field observations in the NAC region using towed electrodes. In 1993, electrode measurements from the Tower Transport Meter (Sanford, unpublished manuscript) found $\overline{\boldsymbol{u}}$ velocities of similar magnitude to the EFFs both in the core of the NAC and in the nearby eddying recirculation region.

6.2. Integral Scales

One measure of turbulent structures is provided by autocorrelation sequences of Lagrangian velocities. Although the large sample size used by Zhang et al. (2001, from 100 floats) for isopycnal $\boldsymbol{u}_{\mathrm{RAF}}$ cannot be improved by our observations, it is of great dynamical interest what the scales are for barotropic flow.

Autocorrelation sequences $r(\tau)$ were calculated by a convolution in the time domain for all valid data points. Gaps in the time-series prevented use of Fourier transform techniques. Each lag-correlation was divided by the length of the entire sequence N, in in analogy to a 'biased' estimate of the autocorrelation sequence (Percival and Walden, 1993). This reduces uncertainty at large lags by normalizing with N instead of $N - |\tau|$, thus biasing

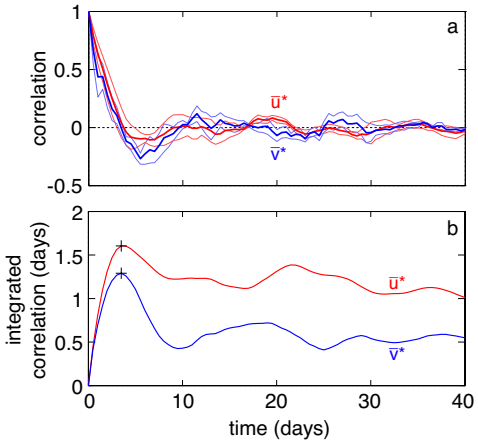

Figure 8: (a) Autocorrelation sequences of $\overline{u}^*$ (red) and $\overline{v}^*$ (blue), with the 95% confidence limits given by the light-colored lines. (b) Cumulative integral of the autocorrelation sequences in (a), with the integral time-scales marked by a black +.

r towards zero. The autocorrelation sequence was then averaged across floats (Figure 8a).

From the autocorrelation sequence, the integral time-scale Γ and integral length-scale (L) are defined as (Taylor, 1921)

$$\Gamma = \int_0^{\tau_0} r(\tau)\,\mathrm{d}\tau \qquad \text{and} \qquad L = \Gamma \left\langle u'^2 \right\rangle^{1/2}$$

where τ_0 is the first zero-crossing of $r(\tau)$, $\langle\,\rangle$ indicates a temporal average, and $'$ indicates a perturbation about a temporal average. The theory used to calculate this assumes that the flow field is stationary, homogeneous, and without any mean flow. Though these assumptions are overly restrictive in most oceanographic regions, it is common to use these equations even with a mean background velocity and strong variability (Bracco et al., 2000; LaCasce and Bower, 2000). For calculating integral scales of $\overline{\boldsymbol{u}}^*$, we note that, although EFFs are not advected by $\overline{\boldsymbol{u}}^*$, $\overline{\boldsymbol{u}}^*$ is intrinsically linked dynamically to the local velocity field and so this is a reasonable if not exact approach to estimating depth-averaged integral scales.

The integral time-scales of $\overline{u}^*$ and $\overline{v}^*$ are 1.6 and 1.3 days, with corresponding length-scales of 28 and 15 km. The errors in Γ are caused by uncertainty in r, and errors in L are caused by those in Γ and in $\left\langle \overline{\boldsymbol{v}^*}' \right\rangle^2$. Despite estimating the confidence level of these scales with standard methods (0.4 days and 5–10 km), we expect that the small sample size gives rise to even larger uncertainty in these values. The corresponding length-scales for $\overline{u}$ and $\overline{v}$ are 34 and 18 km.

The results for $\overline{\boldsymbol{u}}^*$ can be compared with the results for $\boldsymbol{u}_{\mathrm{RAF}}$: Γ of 2.0 and 1.6 days, and L of 53 and 28 km for the u and v components, respectively, with similar confidence limits as for $\overline{\boldsymbol{u}}^*$. These values are consistent with the isotropic values that Zhang et al. (2001) calculated of $\Gamma = 2.2 \pm 1.0$ days and $L = 28 \pm 14$ km, after removal of the mean velocity field in 1/2° bins. The larger L for u_{RAF} compared to Zhang et al. (2001) suggests that the fast eastward flow sampled by all EFFs results in the length-scale of u being biased large. Otherwise, the EFF scales agree with the results of Zhang et al. (2001).

In general, time-scales for $\boldsymbol{u}_{\mathrm{RAF}}$ are larger than those for $\overline{\boldsymbol{u}}^*$, while the length-scales are shorter. This is expected, because barotropic motion has faster response times and short spatial scales than baroclinic motion (Pérez-Brunuis et al., 2004). The $\overline{\boldsymbol{u}}^*$ integral time-scales may be biased high because the floats are advected at the longer time-scales of $\boldsymbol{u}_{\mathrm{RAF}}$. In the NAC region the integral time- and length-scales are much smaller than in other parts of the world's oceans (Krauss et al., 1990).

6.3. Velocity Spectra

Depth-averaged velocity can be influenced by oscillatory motions in the ocean that arise independent of the large-scale flow, such as tidal, inertial, boundary, or planetary waves. Calculating spectra from the three velocities measured by the EFF indicates which features were present during the sampling period.

Because data gaps create significant problems in calculating spectra, velocity spectra can only be calculated from the nearly continuous record of float 9. Since float 9 equilibrated deep (850–900 m) and moved at close to the depth-averaged velocity, the magnitude of $\boldsymbol{u}_{\mathrm{EF}}$ is small and its $\overline{\boldsymbol{u}}^*$ spectrum closely represents that of a particle moving at the depth-averaged velocity.

Spectra were calculated with a multitaper analysis to maximize the low frequencies resolved. Discrete prolate spheroidal tapers (Percival and Walden, 1993) were used with a half-bandwidth chosen as $NW\Delta t = 2$, where N is the length of the time series, Δt is the sampling interval, and $W = j/N\Delta t$ is the frequency resolution of the estimate. Taking the spectra of $(u \mp iv)/\sqrt{2}$ gave rotary

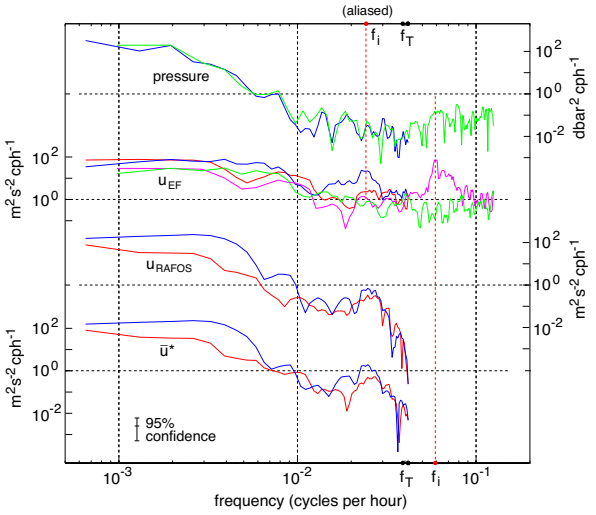

Figure 9: Power spectra for pressure and rotary power spectra for velocities from EFF 9. Rotary spectra are shown with the clockwise (CW) component in red and the counterclockwise (CCW) component in blue for data taken every 12 hours. From top to bottom are: pressure every 4 hours (green) and averaged every 12 hours (blue); $\boldsymbol{u}_{\rm EF}$ every 4 hours (magenta: CW; green: CCW) and averaged every 12 hours; $\boldsymbol{u}_{\rm RAF}$ every 12 hours; and $\overline{\boldsymbol{u}}^*$ every 12 hours. All spectra are normalized by their variance (in parentheses): pressure every 4 hours (1.35×10^3 dbar^2) and every 12 hours (1.24×10^3 dbar^2); $\boldsymbol{u}_{\rm EF}$ every 4 hours (1.59×10^{-3} m^2 s^{-2}) and every 12 hours (6.00×10^{-3} m^2 s^{-2}); $\boldsymbol{u}_{\rm RAF}$ every 12 hours (3.83×10^{-2} m^2 s^{-2}); and $\overline{\boldsymbol{u}}^*$ every 12 hours (3.86×10^{-2} m^2 s^{-2}). The variances are taken of the complex velocity $\boldsymbol{z} = u + iv$. The dots on the lower x-axes show the inertial frequency (red, $f_{\rm i}$) and selected tidal frequencies (black, for the O_1, P_1, and K_1 constituents, $f_{\rm T}$), with the dots at top showing the aliased and direct frequencies as resolved by the 12-hour data sampling. Semi-diurnal tidal frequencies cannot be resolved from 12-hourly RAFOS fixes. The line in the bottom left shows the 95% confidence intervals.

velocity spectra in the clockwise (CW) and counterclockwise (CCW) directions, respectively. The relatively slow sampling rate for $\boldsymbol{u}_{\rm RAF}$ (12 hours) leads to a Nyquist frequency higher than inertial and semi-diurnal tidal frequencies, and so some oceanic motion will be aliased. The EF system, with velocities every 4 hours, does resolve these frequencies directly, though we also use the 12-hour averaged $\boldsymbol{u}_{\rm EF}$ data to quantify the extent of aliasing.

There are no significant peaks in the pressure record at periods shorter than 100 hours (Figure 9). This is expected, as the floats are isobaric and would sample oscillating vertical velocity by rotating about their axis. Vertical motion related to the horizontal flow field would explain the low frequency energy in pressure, whereby vertical drag can displace the floats from their equilibrium float depth. The four-hourly $\boldsymbol{u}_{\rm EF}$ data have a sharp peak at the inertial frequency in the CW rotary component, with no peak in the CCW component, consistent with inertial waves rotating CW in the northern hemisphere. Converting $\boldsymbol{u}_{\rm EF}$ to 12-hourly data by bin averaging aliases this peak to the CCW component, as well as decreasing its magnitude and leaking some power to the CW component. In both the 4-hourly and 12-hourly data the peaks associated with the inertial frequency are statistically significant. Aside from the inertial peak, the background spectra of $u_{\rm EF}$ and $v_{\rm EF}$ is white at periods shorter than 100 hours.

The $\boldsymbol{u}_{\rm RAF}$ spectrum is largest at low frequencies, and there is a small peak at the aliased inertial frequency that is not significant. The combination of $\boldsymbol{u}_{\rm EF}$ and $\boldsymbol{u}_{\rm RAF}$ for $\overline{\boldsymbol{u}}^*$ yields a slightly larger peak at the inertial frequency. Both $\boldsymbol{u}_{\rm RAF}$ and $\overline{\boldsymbol{u}}^*$ have red spectra with most variance at periods longer than 200 hours (roughly 10 days), which is related to the relatively short (45 days) float trajectory that started out in the core of the NAC and then was ejected. The coherence cross-spectrum between $\boldsymbol{u}_{\rm EF}$ and $\boldsymbol{u}_{\rm RAF}$ (not shown) shows that the two signals are only coherent at direct or aliased periods corresponding to periods of 30, 26, and slightly above 24 hours. The latter two peaks are close to the expected periods of diurnal (O_1, P_1, and K_1) tidal constituents.

Though inertial oscillations tend to be have small vertical scales with respect to the depth of the water column in the open ocean, these signals are apparent in the depth averaged data. This suggests that wind-forcing, especially the stormy weather during the float deployment, input energy into barotropic inertial oscillations.

7. Conclusion

The EFF was developed to make electric field observations from a RAFOS float in order to indirectly measure vertically-averaged velocity. It was deployed in a field trial in the North Atlantic Current, contemporaneous with other field programs that provide independent measurements for verification. We find:

- The EFF measurements are consistent between pairs of instruments and with independent velocities, and are accurate to 0.02–0.03 m s^{-1}.

- Fast depth-averaged velocities were measured. In the core of the NAC, depth-averaged velocities were consistently 0.5 m s^{-1}, with maxima of 0.6–0.9 m s^{-1}. Eddies and recirculations adjacent to the NAC showed depth-averaged velocities of 0.2–0.4 m s^{-1}.

- The float at 900 dbar moved at close to the depth-averaged velocity, while shallower floats moved faster because of the contribution from surface intensified baroclinic shear. Depth-averaged velocities contained significant variance at inertial frequencies.

- Integral length-scales and time-scales are slightly smaller for depth-averaged velocities than for float velocities.

In presenting the observational capabilities of the EFF, this manuscript provides scientific results as well as an evaluation of existing sampling technologies and methodologies. The novel combination of electric field measurements and subsurface positioning from RAFOS allows for unique measurements (depth-averaged velocity) with modest expense when deployed near existing sound sources. Since RAFOS tracking is well-proven, RAFOS floats are being used in current observational programs (Gille et al., 2007; Bower et al., 2009) and the technology is being added to more recent float bodies for underwater tracking (Klatt et al., 2005). A more recently developed float with electric fields, the EM-APEX, (Sanford et al., 2007) has programmable sampling patterns that can adjust to the process of interest — from 10-day drifts at depth for standard ARGO floats to continuous profiling (D'Asaro et al., 2007). Although the EM-APEX lacks subsurface acoustic tracking, its absolute motion can be calculated by GPS fixes upon surfacing or by nearby shipboard ADCP profiles. For interpreting EM-APEX floats or other instruments based on motional induction, our treatment of the EFF provides a template. Scientifically, our results suggest that sampling regions with strong barotropic eddies, such as the subpolar North Atlantic here or the Antarctic Circumpolar Current, requires frequent sampling to resolve inertial barotropic motion.

Acknowledgements. The EFF was engineered and operated principally by R. Drever and J. Dunlap of APL/UW, while their deployment in the NAC was kindly performed by Sandy Fontana (URI) amongst other RAFOS deployments for Tom Rossby's NAC float program. The RAFOS tracking was performed by Kathy Schulz-Tokos. NSF supported the developments and deployments. Z.B. Szuts was funded by a National Defense Science and Engineering Graduate Fellowship and by NSF grant OCE-0552139. T. Sanford was supported by NSF grant OCE-9000143. The authors are grateful to T. Rossby for his encouragement and invitations to participate on his cruises in the NAC.

Anderson-Fontana, S., Prater, M., Rossby, T.H., 1996. RAFOS float data report of the North Atlantic Current study 1993–1995. Tech. Rep. 96-4. Graduate School of Oceanography, University of Rhode Island. 241 pp.

Boebel, O., Barron, C., 2003. A comparison of in-situ float velocities with altimeter derived geostrophic velocities. Deep-Sea Res. Pt. II 50, 119–139.

Bower, A.S., Lozier, M.S., Gary, S.F., Böning, C.W., 2009. Interior pathways of the North Atlantic meridional overturning circulation. Nature 459, 243–248.

Bower, A.S., Lozier, S., Gary, S., 2011. Export of Labrador Sea Water from the subpolar North Atlantic: a Lagrangian perspective. Deep-Sea Res. Pt. II in press.

Bower, A.S., Rossby, T.H., 1989. Evidence of cross-frontal exchange processes in Gulf Stream meanders based on isopycnal RAFOS float data. J. Phys. Oceanogr. 19, 1177–1190.

Bower, A.S., von Appen, W.J., 2008. Interannual variability in the pathways of the North Atlantic Current over the Mid-Atlantic Ridge and the impact of topography. J. Phys. Oceanogr. 38, 104–120.

Bracco, A., LaCasce, J.H., Provenzale, A., 2000. Velocity probability density functions for oceanic floats. J. Phys. Oceanogr. 30, 461–474.

Caniaux, G., Prieur, L., Giordani, H., Hernandez, F., Eymard, L., 2001. Observations of the circulation in the Newfoundland Basin in winter 1997. J. Phys. Oceanogr. 31, 689–710.

Carr, M.E., Rossby, T.H., 2001. Pathways of the North Atlantic Current from surface drifters and subsurface floats. J. Geophys. Res. 106, 4405–4419.

Chave, A.D., Luther, D.S., 1990. Low-frequency, motionally induced electromagnetic fields in the ocean: 1. Theory. J. Geophys. Res. 95, 7185–7200.

Clarke, R.A., Hendry, R.M., Yashayaev, I., 1998. A western boundary current meter array in the North Atlantic near 42°N, in: WOCE Newsletter, WOCE International Program Office, Southampton, United Kingdom. pp. 33–34.

Clarke, R.A., Hill, H.W., Reiniger, R.F., Warren, R.F., 1980. Current system south and east of the Grand Banks of Newfoundland. J. Phys. Oceanogr. 10, 25–65.

D'Asaro, E.A., Sanford, T.B., Niiler, P.P., Terrill, E.J., 2007. Cold wake of Hurricane Frances. Geophys. Res. Lett. 34, L15609.

Dietrich, G., Kalle, K., Krauss, W., Siedler, G., 1975. General Oceanography. John Wiley, New York, NY. 626 pp.

Dutkiewicz, S., Rothstein, L., Rossby, T.H., 2001. Pathways of cross-frontal exchange in the North Atlantic Current. J. Geophys. Res. 106, 26917–26928.

Flosadóttir, Á.H., Larsen, J.C., Smith, J.T., 1997. Motional induction in North Atlantic circulation models. J. Geophys. Res. 102, 10353–10372.

Gille, S.T., Speer, K., Ledwell, J.R., Garabato, A.N.G., 2007. Mixing and stirring in the Southern Ocean. EOS T. Am. Geophy. Un. 88, 382.

Johns, W.E., Shay, T.J., Bane, J.M., Watts, D.R., 1995. Gulf Stream structure, transport, and recirculation near 68°W. J. Geophys. Res. 100, 817–838.

Kearns, E.J., Rossby, T.H., 1998. Historical position of the North Atlantic Current. J. Geophys. Res. 103, 15509–15524.

Klatt, O., Boebel, O., Núñez Riboni, I., Fahrbach, E., 2005. Float observations within the Weddell sea. CLIVAR Exchanges 35, 43–46.

Krauss, W., 1986. The North Atlantic Current. J. Geophys. Res. 91, 5061–5074.

Krauss, W., Döscher, R., Lehmann, A., Viehoff, T., 1990. On eddy scales in the eastern and northern North Atlantic Ocean as a function of latitude. J. Geophys. Res. 95, 18049–18056.

Krauss, W., Fahrbach, E., Aitsam, A., Elken, J., Koske, P., 1987. the North Atlantic Current and its associated eddy field southeast of the Flemish Cap. Deep-Sea Res. 34, 1163–1185.

LaCasce, J.H., Bower, A., 2000. Relative dispersion in the subsurface North Atlantic. J. Mar. Res. 58, 863–894.

Laske, G., Masters, G., 1997. A global digital map of sediment thickness. EOS T. Am. Geophy. Un. 78, F483.

Lherminier, P.D., 1998. Convection profonde en Mer du Groenland: Étude expérimentale des phases de préconditionnement et de mélange. Ph.D. thesis. Université Paris 6.

Luther, D.S., Chave, A.D., 1993. Observing integrating variables in the ocean, in: Proceedings of the 7th Annual 'Aha Huliko'a Hawai'ian Winter Workshop on Statistical Methods in Physical Oceanography, University of Hawai'i. pp. 103–129.

Macmillan, S., Maus, S., Bondar, R., Chambodut, A., Golovkov, V., Holme, R., Langlais, B., Lesur, V., Lowes, F., L uhr, H., Mai, W., Mandea, M., Olsen, N., Rother, M., Sabaka, T.J., Thomson, A., Wardinski, I., 2003. Ninth generation International Geomagnetic Reference Field released. Geophys. J. Int. 155, 1051–1056.

Mann, C.R., 1967. The termination of the Gulf Stream and the beginning of the North Atlantic Current. Deep-Sea Research 14, 337–359.

Meinen, C.S., 2001. Structure of the North Atlantic current in stream-coordinates and the circulation in the Newfoundland Basin. Deep-Sea Res. Pt. I 48, 1553–1580.

Meinen, C.S., Watts, D.R., 2000. Vertical structure and transport on a transect across the North Atlantic current near 42°N: Time series and mean. J. Geophys. Res. 105, 21869–21891.

Meinen, C.S., Watts, D.R., Clarke, R.A., 2000. Absolutely referenced geostrophic velocity and transport on a section across the North Atlantic current. Deep-Sea Res. Pt. I 47, 309–322.

Percival, D.B., Walden, A.T., 1993. Spectral Analysis for Physical Applications. Cambridge University Press. 583 pp.

Pérez-Brunuis, P., Rossby, T.H., Watts, D.R., 2004. Absolute transports of mass and temperature for the North Atlantic Current-subpolar front system. J. Phys. Oceanogr. 34, 1870–1883.

Rhein, M., Kieke, D., Hüttl-Kabus, S., Roessler, A., Mertens, C., Miessner, R., Klein, B., Böning, C.W., Yashayaev, I., 2011. Deep water formation, the subpolar gyre, and the meridional overturning circulation in the subpolr North Atlantic. Deep-Sea Res. Pt. II .

Rossby, T.H., 1996. The North Atlantic Current and surrounding waters: at the crossroads. Reviews of Geophysics 34, 463–481.

Rossby, T.H., Dorson, D., Fontaine, J., 1986. The RAFOS system. J. Atmos. Oceanic Technol. 3, 672–679.

Salmon, R., 1980. Baroclinic instability and geostrophic turbulence. Geophysical and Astrophysical Fluid Dynamics 15, 167–211.

Sanford, T.B., 1971. Motionally induced electric and magnetic fields in the sea. J. Geophys. Res. 76, 3476–3492.

Sanford, T.B., 1986. Recent improvements in ocean current measurement from motional electric fields and currents, in: Proceedings of the IEEE Third Working Conference on Current Measurement, pp. 65–76.

Sanford, T.B., Drever, R.G., Dunlap, J.H., 1978. A velocity profiler based on the principles of geomagnetic induction. Deep-Sea Res. 25, 183–210.

Sanford, T.B., Drever, R.G., Dunlap, J.H., 1985. An acoustic Doppler and electromagnetic velocity profiler. J. Atmos. Oceanic Technol. 2, 110–124.

Sanford, T.B., Drever, R.G., Dunlap, J.H., 1995. Barotropic ocean velocity observations from an electric field float, a modified RAFOS float, in: Anderson, S., Appell, G., Williams, A.J.r. (Eds.), Proceedings of the IEEE Fifth Working Conference on Current Measurement, William S. Sullword Publishing, Taunton, MA. pp. 163–168. IEEE Catalog No. 95CH35734.

Sanford, T.B., Dunlap, J.H., Verrall, J., Osse, T.J., Drever, R.G., Bartlett, A.C., Allison, M.D., 1993. The Electric Field Float and its Sea Test on R/V *Endeavor* Cruise 230. Technical Report 9314. Applied Physics Lab, University of Washington. 41 pp.

Sanford, T.B., Price, J.F., Girton, J.B., 2011. Upper ocean response to Hurricane Frances (2004) observed by profiling EM-APEX floats. J. Phys. Oceanogr. 41, 1041–1056.

Sanford, T.B., Price, J.F., Girton, J.B., Webb, D.C., 2007. Highly resolved observations and simulations of the ocean response to a hurricane. Geophys. Res. Lett. 34, L13604.

Schmitz, Jr, W.J., McCartney, M.S., 1993. On the North Atlantic circulation. Rev. Geophys. 31, 29–49.

Schott, F.A., Zantopp, R., Stramma, L., Dengler, M., Fischer, J., Wibaux, M., 2004. Circulation and deep-water export at the western exit of the subpolar North Atlantic. J. Phys. Oceanogr. 34, 817–843.

Smith, W.H.F., Sandwell, D.T., 1997. Global seafloor topography from satellite altimetry and ship depth soundings. Science 277, 1957–1962.

Szuts, Z.B., 2004. Electric Field Floats in the North Atlantic Current: Validation and Observations. Technical Report APL-UW 0405. Applied Physics Lab, University of Washington.

Szuts, Z.B., 2010. The relationship between ocean velocity and motionally-induced electrical signals, part 2: in the presence of topographic slopes. J. Geophys. Res. 115.

Szuts, Z.B., 2012. Using motionally-induced electric fields to indirectly measure ocean velocity: instrumental and theoretical developments. Prog. Oceanogr. 96, 108–127.

Taylor, G.I., 1921. Diffusion by continuous movement. Proc. London Math. Soc. 21, 196–212.

Tucholke, B.E., 1986. Structure of basement and distribution of sediments in the western North Atlantic Ocean, in: Vogt, P.R., Tucholke, B.E. (Eds.), The Western North Atlantic Region. Geological Society of America, Inc., Boul-

der, CO, pp. 331–340.
Tyler, R.H., Mysak, L.A., Oberhuber, J.M., 1997. Electromagnetic fields generated by a 3-D global ocean circulation. J. Geophys. Res. 102, 5531–5551.
Webb, D.C., Worthington, L.V., 1968. Measurements of vertical water movement in the Cayman Basin. Deep-Sea Res. 15, 609–612.
Zhang, H.M., Prater, M.D., Rossby, T.H., 2001. Isopycnal lagrangian statistics from the North Atlantic Current RAFOS float observations. J. Geophys. Res. 106, 13817–13836.